*J. Fluid Mech.* (2022), *vol*. 952, A21, doi:10.1017/jfm.2022.915

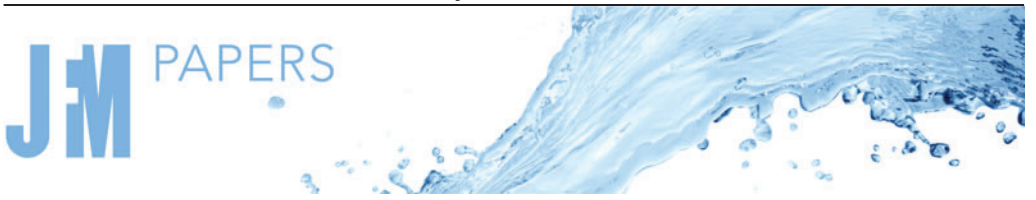

# Dissimilar turbulent heat transfer enhancement by Kelvin–Helmholtz rollers over high-aspect-ratio longitudinal ribs

**Y. Kuwata**†

Department of Mechanical Engineering, Osaka Metropolitan University, Sakai, Osaka 599-8531, Japan

(Received 19 April 2022; revised 18 October 2022; accepted 22 October 2022)

Passive heat transfer enhancement by spanwise rollers associated with the Kelvin–Helmholtz instability was studied through direct numerical simulations of high-aspect-ratio longitudinal ribs at the friction Reynolds number 300. The temperature was treated as a passive scalar with Prandtl number unity to discuss the similarity between the heat and momentum transfer. The results reveal that the high-aspect-ratio longitudinal ribs lead to a favourable breakdown of the Reynolds analogy, that is, the enhancement of the heat transfer rate surpasses that of the frictional resistance. The favourable breakdown of the Reynolds analogy can be attributed to the enhanced turbulent heat flux compared with the Reynolds shear stress, whereas the rib-induced secondary flow plays a role in reducing the favourable breakdown of the Reynolds analogy. The conditional average statistics reveal that the high-pressure region accompanied by the spanwise rollers suppresses the spanwise roller-induced sweep and ejection motions, leading to smaller Reynolds shear stress than for the turbulent heat flux.

**Key words:** turbulence simulation, turbulent convection, mixing enhancement

## 1. Introduction

Heat transfer enhancement by passive or active control is a critical research topic. For passive control, adding wall roughness to heat transfer surfaces, such as transverse/longitudinal ribs (Liou, Hwang & Chen 1993; Murata & Mochizuki 2001) and dimples/protrusions (Mahmood, Sabbagh & Ligrani 2001; Hwang *et al.* 2008), is a simple and widely used control technique. It is well known that there is a similarity between the momentum and heat transfer because the governing equations for scalar and flow fields are similar, with the exception of the pressure term. When the diffusivities for flow and scalar fields are identical, the ratio of the Stanton number $S_t$ to the skin friction

† Email address for correspondence: kuwata@me.osakafu-u.ac.jp

coefficient $C_f$, which is referred to as the Reynolds analogy factor, $RA = 2S_t/C_f$, is close to unity for a smooth wall-bounded flow. However, the wall roughness generally breaks the similarity between the momentum and heat transfer unfavourably, i.e. augmentation of $C_f$ is larger than that of $S_t$ for rough surfaces. This phenomenon is supported by many experimental data (Dipprey & Sabersky 1963; Kays & Crawford 1993; Bons 2002), theoretical analysis (Katoh, Choi & Azuma 2000) and direct numerical simulations (DNS) data (Forooghi, Stripf & Frohnapfel 2018; MacDonald, Hutchins & Chung 2019; Peeters & Sandham 2019; Kuwata 2021). The key factor that causes an unfavourable breakdown of the Reynolds analogy is an increased pressure drag acting on roughness elements. The pressure drag directly increases $C_f$ but not $S_t$ because no corresponding mechanisms exists for an increase in the heat transfer rate (Katoh *et al.* 2000; MacDonald *et al.* 2019; Kuwata 2021). Therefore, the breakdown of the Reynolds analogy can be circumvented to some degree by the use of the roughness that does not offer the pressure drag – for example, obstacles aligned with the flow directions (Stalio & Nobile 2003; Jin & Herwig 2014; Stroh *et al.* 2020). Recent theoretical studies by Alben (2017) and Motoki, Kawahara & Shimizu (2018) demonstrated the possibility of an optimized shear flow with a much higher heat transfer rate than skin friction, i.e. enabling the favourable breakdown of the Reynolds analogy. Although the optimized shear flows in those studies were driven by an arbitrary body force, it was demonstrated that a heat transfer rate higher than skin friction can be realized by Coriolis force for shear flows subjected to system rotation (Brethouwer 2021) and buoyancy force for mixed convection with unstable stratification (Pirozzoli *et al.* 2017). Nevertheless, to the best of the author's knowledge, there is no report on the passive control technique with a roughness obstacle that yields significant favourable breakdown of the Reynolds analogy.

In contrast to the passive control, several active control techniques successfully achieve favourable breakdown of the Reynolds analogy. Specifically, travelling-wave-like local blowing/suction from the wall is one of the most outstanding techniques to achieve favourable dissimilar heat transfer enhancement (Hasegawa & Kasagi 2011; Yamamoto, Hasegawa & Kasagi 2013; Kaithakkal, Kametani & Hasegawa 2020). Notably, the turbulent structure near the wall with travelling-wave-like local blowing/suction is visually similar to the turbulent structure modulated by the spanwise rollers associated with the Kelvin–Helmholtz (K–H) instability, which we encounter commonly in porous wall turbulence (Breugem, Boersma & Uittenbogaard 2006; Suga *et al.* 2010; Kuwata & Suga 2016*a*, 2017). This serves as a motivation to exploit the spanwise rollers for the heat transfer control. The aim of the present DNS study is to open the way for the favourable breakdown of the Reynolds analogy by the spanwise rollers. The high-aspect-ratio longitudinal ribs aligned with the flow directions, which can induce the spanwise rollers associated with the K–H instability, were considered in the study. We performed DNS of turbulent heat transfer over high-aspect-ratio longitudinal ribs with Prandtl number unity, and discussed the possibility of the favourable breakdown of the Reynolds analogy by the spanwise rollers in a passive manner.

## 2. DNS methodology

Figure 1 illustrates a schematic of a turbulent open-channel flow over rib roughness in which the streamwise-aligned longitudinal ribs were mounted regularly at the bottom wall. The computational box was $L_x = 6.0H$ and $L_z = 3.3H$, with $H$ being the clear channel height. The flow was periodic in the streamwise ($x$) and spanwise ($z$) directions, and simulations were run at a constant streamwise pressure difference. The friction Reynolds

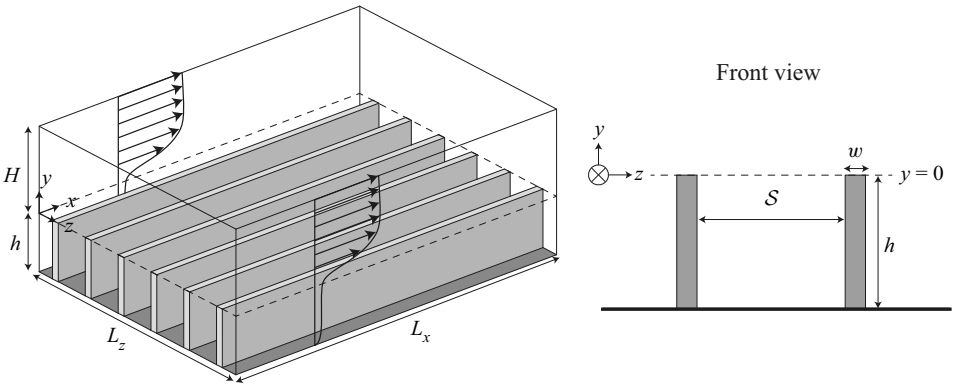


Figure 1. Configuration of a turbulent open-channel flow over longitudinal ribs.

number for the clear flow region ($0 < y < H$) was fixed at $Re_\tau = u_\tau H/\nu = 300$, where $u_\tau$ is the average friction velocity at the position of the rib crest ($y = 0$), and $\nu$ is the kinematic viscosity. An incompressible fluid was considered, and the fluid Prandtl number $Pr$ was assumed to be unity. Constant wall temperature $T_w$ was specified at the surfaces of the ribs and bottom wall, whereas slip and adiabatic boundary conditions were imposed for the top boundary face. The heat transfer is driven by volumetric heat generation $q_v$. In this set of heat transfer and fluid flow conditions, the time-averaged momentum and heat transport equations in non-dimensional form were similar (Kasagi *et al.* 2010; Hasegawa & Kasagi 2011). Specifically, the normalized heat generation in the energy equation corresponds to the normalized mean pressure gradient in the momentum equation. We considered high-aspect-ratio longitudinal ribs with various distances between the neighbouring ribs. The height and width of the rib were $h = 0.67H$ and $w = 0.05h$, respectively, which resulted in aspect ratio $h/w = 20$. The separation between the ribs was varied: $s/h = 0.05$, 0.075, 0.2, 0.45 and 1.2. For reference, we additionally performed smooth-wall simulation with the box of $6.0\,H(x) \times H(y) \times 3.3\,H(z)$.

For the numerical method, in following earlier works (Suga, Chikasue & Kuwata 2017; Kuwata, Tsuda & Suga 2020; Nishiyama, Kuwata & Suga 2020; Kuwata 2021), the three-dimensional 27-velocity multiple-relaxation-time lattice Boltzmann method (LBM) for the flow field was used, whereas the scalar field was simulated by the three-dimensional 19-velocity regularized LBM. The number of grid points was determined as $1080(x) \times 301(y) \times 600(z)$, which yields $\Delta^+ = 1.67$ in all directions, with $\Delta^+$ being the grid spacing normalized by wall unit $\nu/u_\tau$. This resolution is comparable to those used in previous DNS (Kuwata & Suga 2016*a*, 2019; Kuwata & Kawaguchi 2019; Kuwata & Nagura 2020; Kuwata *et al.* 2020). To validate the independence of grid resolution and box size, we performed grid and domain size sensitivity tests for the case $s/h = 0.2$ in which $S_t$ is the largest among the simulation cases. A comparison of the results for $\Delta^+ = 1.67$ and 2.5 confirmed that the differences in $S_t$ and $C_f$ were within 0.7 % and 1.4 %, respectively. Regarding the domain size, we performed DNS with a domain size enlarged by a factor 1.5 in wall-parallel directions, and found that the difference in the maximum peak values of the Reynolds stresses and turbulent heat fluxes was 1.4 % at most. We also confirmed that the enlargement of the domain size yielded a change of less than 0.7 % in $S_t$ and $C_f$.

To discuss the profiles of the turbulence statistics near rib roughness from a macroscopic perspective, we considered a variable averaged over the $x$–$z$ plane and time in the following discussion. Superficial and intrinsic averaging operators for a variable $\phi(x, y, z)$ are

introduced as

$$\langle\phi\rangle(y,t)=\frac{1}{A}\int_x\int_z\phi(x,y,z,t)\,\mathrm{d}x\,\mathrm{d}z,\quad \langle\phi\rangle^f(y,t)=\frac{1}{A_f}\int_x\int_z\phi(x,y,z,t)\,\mathrm{d}x\,\mathrm{d}z, \tag{2.1a,b}$$

where $A=L_xL_z$ is the area of the $x$–$z$ plane, and $A_f$ is the area occupied by the fluid in the $x$–$z$ plane. Therefore, a relationship exists between the superficial and intrinsic plane-averaged values as $\langle\phi\rangle=\varphi\langle\phi\rangle^f$, with the volume fraction of the fluid phase, $\varphi=s/(s+w)$, below the roughness crest ($y<0$), while $\varphi=1$ in the clear flow region ($y>0$) for the geometry presented herein. The deviation from the intrinsic averaged value $\tilde{\phi}(x,y,z,t)$, which is referred to as the dispersion, is

$$\tilde{\phi}(x,y,z,t)=\phi(x,y,z,t)-\langle\phi\rangle^f(y,t). \tag{2.2}$$

We additionally considered the Reynolds decomposition that decomposes a variable into a time-averaged value $\bar{\phi}(x,y,z)$ and its fluctuation $\phi'(x,y,z,t)$ as $\phi(x,y,z,t)=\bar{\phi}(x,y,z)+\phi'(x,y,z,t)$. After a flow had reached a fully developed state, statistical properties were assembled over a period $50H/u_\tau$.

All the quantities in plus units $(\cdot)^+$ are scaled with the average friction velocity $u_\tau$ or average friction temperature $\theta_\tau$. The friction velocity $u_\tau$ was based on the average wall shear stress at the rib crest position, $\tau_w=\rho u_\tau^2$, with $\rho$ denoting the fluid density. The average wall shear stress was calculated using the pressure gradient via the momentum balance in the clear flow region as in Kuwata & Suga (2016*a*, 2017):

$$\tau_wA=\int_0^{L_z}\int_0^{H}\int_0^{L_x}\left(-\frac{\partial\bar{p}}{\partial x}\right)\mathrm{d}x\,\mathrm{d}y\,\mathrm{d}z, \tag{2.3}$$

where $A=L_xL_z$ is the $x$–$z$ plane area. Analogous to the friction velocity, the friction temperature $\theta_\tau$ was based on the average wall heat flux evaluated at the rib crest position $q_w=\rho c u_\tau\theta_\tau$, with $c$ denoting the specific heat. The average wall heat flux was calculated by a heat source for volumetric heating, $q_v$, via the energy balance in the clear flow region,

$$q_wA=\int_0^{L_z}\int_0^{H}\int_0^{L_x}q_v\,\mathrm{d}x\,\mathrm{d}y\,\mathrm{d}z, \tag{2.4}$$

where the volumetric heat source $q_v$ has a non-zero constant value in the fluid phase but value zero in the solid phase.

## 3. Results and discussion

To discuss briefly augmentations of heat and momentum transfer by the rib roughness, we investigate the skin friction coefficient $C_f$ and Stanton number $S_t$, which are given as $C_f=2/(U_b^+)^2$ and $S_t=1/(U_b^+\Theta_a^+)$, respectively. Here, $U_b$ and $\Theta_a$ are the bulk mean velocity and arithmetic mean temperature in the clear flow region ($y>0$), which are defined as

$$U_b=\frac{1}{H}\int_0^H\langle\bar{u}\rangle\,\mathrm{d}y,\quad \Theta_a=\frac{1}{H}\int_0^H\langle\bar{\theta}\rangle\,\mathrm{d}y, \tag{3.1a,b}$$

Note that for the present definition, the identical inner-scaled mean velocity and temperature profiles give $C_f=2S_t$. Augmentations of $S_t$ and $C_f$ from the corresponding

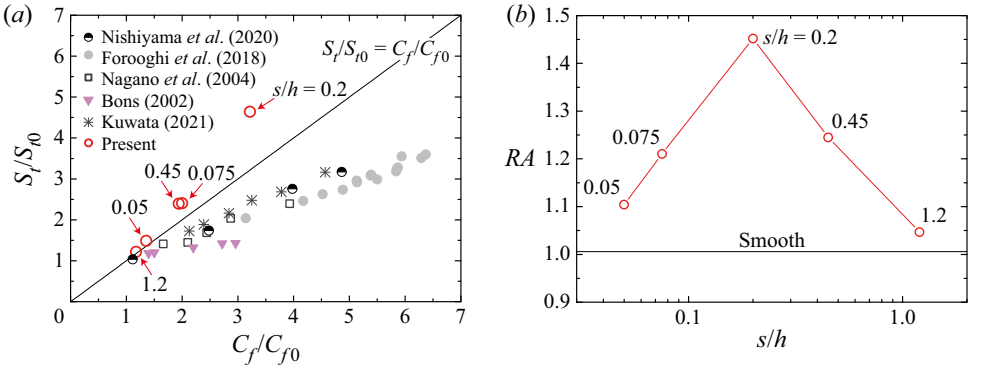


Figure 2. (*a*) Stanton number $S_t/S_{t0}$ against the skin friction coefficient $C_f/C_{f0}$, and (*b*) Reynolds analogy factor $RA$ against the rib separation $s/h$. The DNS data for random cone roughness (Forooghi *et al.* 2018), three-dimensional irregular rough surfaces (Kuwata 2021), two-dimensional transverse bar roughness (Nagano *et al.* 2004) and porous walls (Nishiyama *et al.* 2020), and experimental data for turbine roughness (Bons 2002), are included. The thin line in (*a*) indicates $S_t/S_{t0} = C_f/C_{f0}$, and that in (*b*) indicates $RA = 1.007$ for a smooth wall.

smooth wall values $S_{t0}$ and $C_{f0}$ are displayed in figure 2(*a*) along with the DNS data for random cone roughness (Forooghi *et al.* 2018), three-dimensional irregular rough surfaces (Kuwata 2021), two-dimensional transverse bar roughness (Nagano, Hattori & Houra 2004), porous walls (Nishiyama *et al.* 2020), and experimental data for turbine roughness (Bons 2002). Additionally, figure 2(*b*) displays the Reynolds analogy factor $RA = 2S_t/C_f$, which quantifies the similarity between the heat and momentum transfer. For the present definition, the $RA$ value is exactly unity when the Reynolds analogy holds because the identical inner-scaled mean velocity and temperature profiles give $C_f = 2S_t$.

In figure 2(*a*), all the reference data are below a line $S_t/S_{t0} = C_f/C_{f0}$, which is an expected result that indicates the unfavourable breakdown of the Reynolds analogy by the passive controls. By contrast, the present results are all above the line $S_t/S_{t0} = C_f/C_{f0}$, which indicate that the augmentation of $S_t$ from the smooth wall value is larger than that of $C_f$. This favourable breakdown of the Reynolds analogy is quantified by the $RA$ value in figure 2(*b*), which reveals that the $RA$ value is close to unity for the smooth wall case, whereas the $RA$ value exceeds unity for the rib cases. It is found that the $RA$ value attains the maximum peak value $RA = 1.45$ for $s/h = 0.2$, where the favourable breakdown of the Reynolds analogy is the most pronounced. Note that for the present study, global quantities such as $Re_\tau$, $C_f$, $S_t$ and $RA$ were calculated based on the assumption that the rib crest position was an origin of the $y$-coordinate. However, there are other possible choices for the origin, and alternative candidates include the rib bottom and level at the zero plane displacement (Pokrajac *et al.* 2006). Accordingly, global quantities are affected significantly by the choice of the origin. However, it was confirmed that the $RA$ value, which quantifies the similarity between the heat and momentum transfer, was unaffected by the choice of the origin, ensuring the occurrence of the favourable breakdown of the Reynolds analogy. For example, when we consider the rib bottom as the origin for $s/h = 0.2$, $C_f$ is increased by a factor 3.8, but a change of 2.7 % is observed in $RA$.

To identify the heat flow changes occurring due to the presence of the high-aspect-ratio longitudinal ribs, the time–mean velocity and temperature averaged over the $x$–$z$ plane are shown in figure 3. For the smooth wall case, mean velocity $U^+$ and temperature $\Theta^+$ are almost indistinguishable, whereas a significant deviation can be observed for the

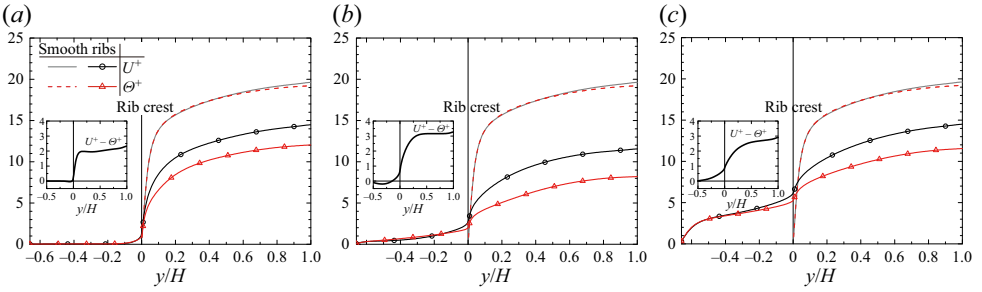


Figure 3. Comparison of mean velocity and temperature profiles for (*a*) $s/h = 0.075$, (*b*) $s/h = 0.2$, and (*c*) $s/h = 0.45$. Insets show the difference in the mean velocity and temperature.

rib cases. Additionally, for rib cases, owing to the increased heat and momentum transfer, the profiles of $U^+$ and $\Theta^+$ are lower than the corresponding smooth wall results. Notably, the decreases in the $\Theta^+$ profiles with respect to the smooth wall results are larger than those in the $U^+$ profiles, suggesting the occurrence of the breakdown of the Reynolds analogy. Another observation from the insets is that the detachment between the $\Theta^+$ and $U^+$ profiles occurs mainly near the rib crest, suggesting that the flow modification near the rib crest is the root cause of the favourable breakdown of the Reynolds analogy.

To obtain a physical understanding of the favourable breakdown of the Reynolds analogy, the momentum and energy budgets were considered. Applying the $x$–$z$ plane and time averaging to the momentum and energy equations for an incompressible fluid, the double-averaged equations non-dimensionalized with $u_\tau$ and $\theta_\tau$ can be derived for the present flow system as (Kuwata 2021)

$$C_u - \frac{1}{H}\int_{-h}^{y} \varphi \,\mathrm{d}y = \frac{\partial \langle \bar{u} \rangle^+}{\partial y^+} - \langle \overline{u'v'} \rangle^+ - \langle \tilde{\bar{u}}\, \tilde{\bar{v}} \rangle^+ + \int_{y^+}^{0} f_x^+ \,\mathrm{d}y^+, \tag{3.2}$$

$$C_\theta - \frac{1}{H}\int_{-h}^{y} \varphi \,\mathrm{d}y = \frac{\partial \langle \bar{\theta} \rangle^+}{\partial y^+} - \langle \overline{v'\theta'} \rangle^+ - \langle \tilde{\bar{v}} \tilde{\bar{\theta}} \rangle^+ + \int_{y^+}^{0} s_w^+ \,\mathrm{d}y^+, \tag{3.3}$$

where the constants of integration on the left-hand sides of (3.2) and (3.3) are obtained from the boundary conditions (zero shear stress and zero heat flux) at $y = H$ as

$$C_u = C_\theta = \frac{h}{H}\frac{s}{s+w} + 1. \tag{3.4}$$

In (3.2) and (3.3), the turbulent fluxes of $R_{12} = \langle \overline{u'v'} \rangle$ and $H_2 = \langle \overline{v'\theta'} \rangle$ are the plane-averaged Reynolds stress and turbulent heat flux, respectively. The spatial averaging produces the dispersive fluxes, namely the dispersive covariance $\mathcal{T}_{12} = \langle \tilde{\bar{u}}\, \tilde{\bar{v}} \rangle$ and the dispersion heat flux $\mathcal{H}_2 = \langle \tilde{\bar{v}}\, \tilde{\bar{\theta}} \rangle$. Additionally, the spatial averaging produces contribution terms by the viscous drag term $f_x$ and wall heat transfer term $s_w$, which are given as

$$f_x = \frac{\nu}{A}\int_L \left(-n_k \frac{\partial \bar{u}}{\partial x_k}\right) \mathrm{d}\ell, \tag{3.5}$$

$$s_w = \frac{\alpha}{A}\int_L \left(-n_k \frac{\partial \bar{\theta}}{\partial x_k}\right) \mathrm{d}\ell, \tag{3.6}$$

where $\alpha$ is the thermal diffusivity, $L$ represents the obstacle perimeter within an averaging $x$–$z$ plane, $\ell$ represents circumferential length of obstacle, and $n_k$ is the unit normal vector

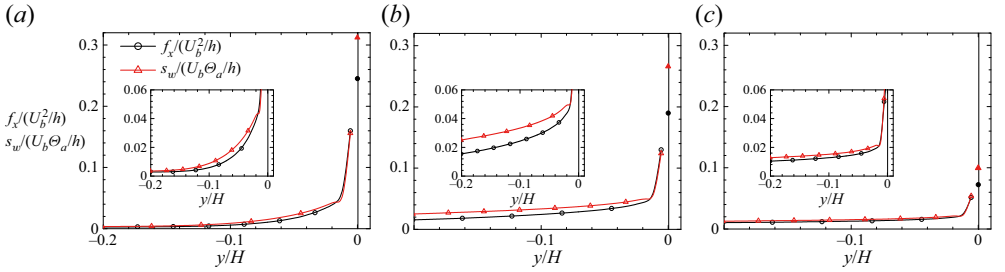


Figure 4. Comparison of the wall-integration terms $f_x/(U_b^2/h)$ and $s_w/(U_b\Theta_a/h)$ for (*a*) $s/h = 0.075$, (*b*) $s/h = 0.2$, and (*c*) $s/h = 0.45$. Insets display enlarged profiles below the rib crest. The closed symbols represent the wall-integration terms at the top of the ribs.

pointing outwards from the fluid to the solid phase. Note that the wall-integration terms represent contributions by the wall shear stress or the wall heat flux at the rib and bottom wall surfaces, whereas the first terms on the right-hand sides of (3.2) and (3.3) account for the molecular diffusion effects driven by the gradients of the $x$–$z$-plane-averaged velocity and temperature, respectively. Hence the wall-integration terms are zero in the clear flow region, whereas they play an important role in the momentum and heat transfer below the rib crest.

Figure 4 compares the wall-integration terms $f_x/(U_b^2/h)$ and $s_w/(U_b\Theta_a/h)$, which represent the $x$–$z$-plane-averaged skin friction coefficient and Stanton number, respectively. It is observed that the wall-integration terms are significant at the rib top and decrease in magnitude towards the bottom wall. Although the results are not shown here, the wall-integration terms are considerably small near the bottom of the ribs, suggesting that most of the heat and momentum transfers take place near the top of the ribs. Consistent with an inequality for the global skin friction coefficient and Stanton number ($S_t > C_f$), the relation $s_w/(U_b\Theta_a/h) > f_x/(U_b^2/h)$ is retained below the rib crest. Notably, significant disparity between $s_w/(U_b\Theta_a/h)$ and $f_x/(U_b^2/h)$ can be found at the top of the ribs, and the heat transfer considerably outweighs the momentum transfer at the rib top. Interestingly, the wall-integration terms in $y/H < 0.02$ do not monotonically increase with rib separation $s/h$, owing to a result of two competing effects. An increase in $s/h$ enables the fluid to flow easily below the rib crest, resulting in increased local wall shear stress and local wall heat flux. In contrast, an increase in $s/h$ decreases the total surface area of the ribs, resulting in decreases in total wall shear stress and total wall heat flux. Given that the integrations of $f_x/(U_b^2/h)$ and $s_w/(U_b\Theta_a/h)$ over the rib region ($-h < y < 0$) correspond to $C_f$ and $S_t$, respectively, the maximum values of $C_f$ and $S_t$ attained for $s/h = 0.2$ are considered to be a result of those competing effects.

Figure 5 compares the turbulent and dispersion fluxes for three rib separation cases, $s/h = 0.075$, 0.2 and 0.45. The turbulent fluxes of $R_{12}^+$ and $H_2^+$ are displayed in figures 5(*a–c*), whereas the dispersive fluxes of $\mathcal{T}_{12}^+$ and $\mathcal{H}_2^+$ are shown in figures 5(*d–f*). The dispersive fluxes for the smooth wall case are not shown because they become zero in the absence of the ribs. In figures 5(*a–c*), the profiles of $-R_{12}^+$ and $-H_2^+$ for the smooth wall case are overlapped perfectly, whereas for the rib cases, $-H_2^+$ outweighs $-R_{12}^+$ near the ribs, which contributes to the favourable breakdown of the Reynolds analogy. Regarding the dispersion fluxes in figures 5(*d–f*), $\mathcal{T}_{12}^+$ and $\mathcal{H}_2^+$ are generated by the secondary mean flow between the ribs as shown in figure 6. The counter-rotating two vortex pairs, which is induced by the spanwise inhomogeneity of the turbulent stress

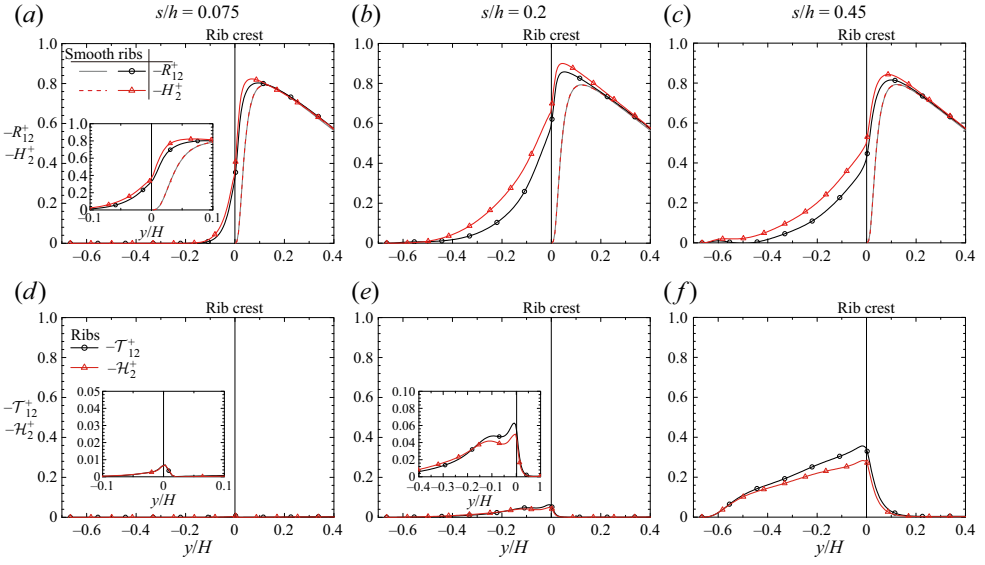


Figure 5. Comparison of turbulent and dispersion fluxes: (*a–c*) compare turbulent fluxes of $R_{12}^+$ and $H_2^+$, and (*d–f*) compare dispersion fluxes of $\mathcal{T}_{12}^+$ and $\mathcal{H}_2^+$.

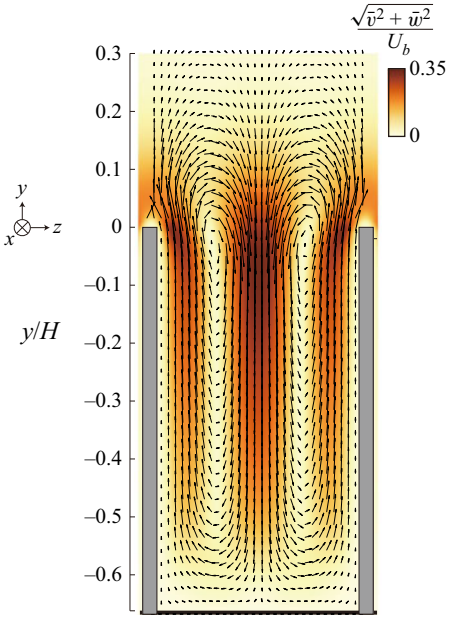


Figure 6. Secondary flow intensity along with the cross-sectional velocity vectors for the case with $s/h = 0.45$.

distribution (Hinze 1973), induce the upward and downward mean flows, convecting the low- and high-momentum (temperature) fluids, respectively. Figure 5(*d–f*) confirms that $-\mathcal{H}_2^+$ is generally smaller than $-\mathcal{T}_{12}^+$, which diminishes the favourable breakdown of the Reynolds analogy. Therefore, the decrease in the *RA* value with $s/h$ for $s/h > 0.2$, as

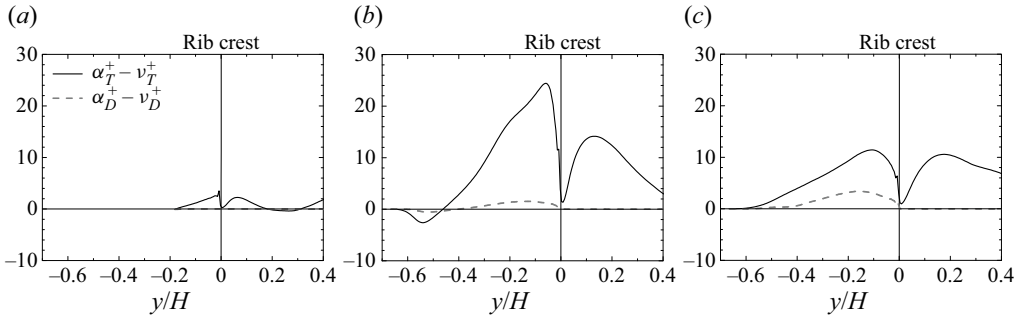


Figure 7. Differences in the turbulent eddy diffusivities $\alpha_T^+ - \nu_T^+$ and the effective diffusivities due to the secondary flows $\alpha_D^+ - \nu_D^+$ for (*a*) $s/h = 0.075$, (*b*) $s/h = 0.2$, and (*c*) $s/h = 0.45$.

shown in figure 2(*b*), can be attributed partly to the smaller dispersion heat flux compared with the dispersive covariance.

The turbulent and dispersion fluxes occupy a large fraction of the total shear stress and heat flux, and have considerable impacts on mean velocity and temperature profiles. However, one needs to keep in mind that the mean velocity and temperature also affect the turbulent and dispersion fluxes themselves. To better understand the heat and momentum transfer due to turbulence and dispersion, we see the effective diffusivities, which are calculated based on the concept of the gradient diffusion hypothesis. The turbulent momentum and thermal diffusivities are defined using the linear eddy viscosity model as

$$\nu_T = -R_{12}\left(\frac{\partial\langle\bar{u}\rangle}{\partial y}\right)^{-1}, \quad \alpha_T = -H_2\left(\frac{\partial\langle\bar{\theta}\rangle}{\partial y}\right)^{-1}. \tag{3.7a,b}$$

Similarly, the dispersion momentum and thermal diffusivities may be defined as (Nakayama, Kuwahara & Kodama 2006; Suga *et al.* 2017)

$$\nu_D = -\mathcal{T}_{12}\left(\frac{\partial\langle\bar{u}\rangle}{\partial y}\right)^{-1}, \quad \alpha_D = -\mathcal{H}_2\left(\frac{\partial\langle\bar{\theta}\rangle}{\partial y}\right)^{-1}. \tag{3.8a,b}$$

To clarify the roles of turbulence and dispersion (secondary mean flow) in the breakdown of the Reynolds analogy, figure 7 displays differences in the turbulent and dispersion diffusivities, i.e. $\alpha_T^+ - \nu_T^+$ and $\alpha_D^+ - \nu_D^+$, respectively. The figure confirms that the turbulent thermal diffusivity $\alpha_T^+$ is generally larger than the turbulent viscosity $\nu_T^+$, i.e. $\alpha_T^+ - \nu_T^+ > 0$, suggesting that turbulence enhances heat transfer more efficiently than momentum transfer. This trend is more pronounced for $s/h = 0.2$ in figure 7(*b*), wherein the *RA* value attains the maximum value. Another observation is that the region where the turbulent diffusivity outweighs the dispersion diffusivity extends further away from the ribs. This implies that relatively large-scale turbulent motions that cause $\alpha_T^+ - \nu_T^+ > 0$ dominate the flows, which will be discussed later. Similar to the turbulent diffusivities, the difference in the dispersion diffusivities, $\alpha_D^+ - \nu_D^+$, exhibits a positive value below the rib crest. Nevertheless, the positive value of $\alpha_D^+ - \nu_D^+$ is much smaller than that of $\alpha_T^+ - \nu_T^+$. Additionally, the considerably smaller $\Theta^+$ in comparison with $U^+$, as shown in figure 3, yields a smaller temperature gradient compared with the mean velocity gradient, resulting in a smaller $-\mathcal{H}_2^+$ value than the $-\mathcal{T}_2^+$ value, as observed in figure 5. Therefore, it can be interpreted that the secondary flow itself does not bring an unfavourable breakdown of the

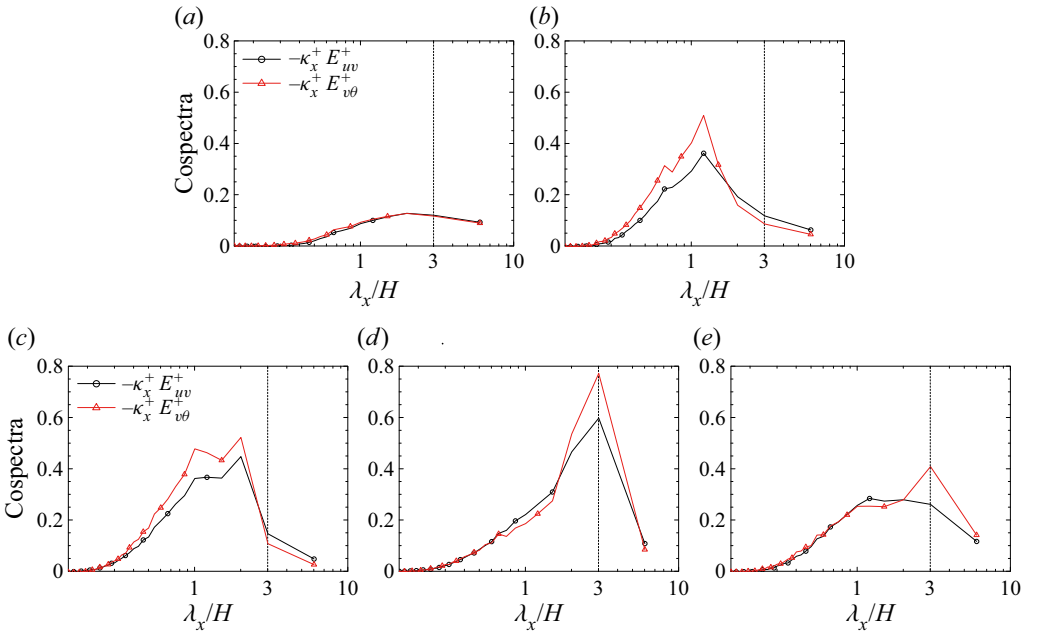


Figure 8. Streamwise one-dimensional pre-multiplied cospectra of the turbulent heat flux and Reynolds shear stress at $y^+ \simeq 10$ for (*a*) the smooth wall case, (*b*) $s/h = 0.05$, (*c*) $s/h = 0.075$, (*d*) $s/h = 0.2$, and (*e*) $s/h = 0.45$.

Reynolds analogy but merely acts to restore the dissimilar heat and momentum transfer caused by turbulent motions.

For a better understanding of the cause of the turbulent heat flux outweighing the Reynolds shear stress, figure 8 presents streamwise one-dimensional cospectra for $-R_{12}$ and $-H_2$ at $y^+ \simeq 10$. The spectra of $-R_{12}$ and $-H_2$ for the smooth wall case in figure 8(*a*) are observed to be very close to each other, whereas the spectra for $-H_2$ generally outweigh those for $-R_{12}$ for the rib case, as shown in figures 8(*b–e*). Additionally, the spectra of $-H_2$ and $-R_{12}$ for the rib cases exhibit a pronounced peak in the long-wavelength region $\lambda_x/H > 1$, and considerable detachment between the energy spectra for $-H_2$ and $-R_{12}$ is observed near the maximum peak location. This implies that the favourable breakdown of the Reynolds analogy is responsible for the turbulent motions that correspond to the maximum spectral peak. Apparently, the maximum peak location tends to shift to a longer-wavelength region with increasing $s/h$, and reaches an asymptotic value $\lambda_x/H \simeq 3$. Notably, the asymptotic wavelength $\lambda_x/H \simeq 3$ corresponds roughly to the characteristic wavelength of the spanwise rollers associated with the K–H instability; see Kuwata & Suga (2017, 2019) Suga *et al.* (2018). They reported that the characteristic wavelength of the spanwise rollers is approximately 2–5.5 times as large as the boundary layer thickness.

Evidence of the spanwise rollers associated with the K–H instability can be found in the two-dimensional cospectra shown in figure 9, where the pre-multiplied two-dimensional cospectra for $-R_{12}$ at $y^+ \simeq 10$ are shown. The spectra for $s/h = 0.05$ in figure 9(*b*) show stronger coherence in the spanwise direction compared with the smooth wall result in figure 9(*a*). An enhancement in the larger spanwise wavelength region is more pronounced with increasing $s/h$ from 0.075 to 0.2 in figures 9(*c*,*d*), whereas the further increase in $s/h$ from 0.2 to 0.45 attenuates the spectra at larger spanwise wavelengths in figures 9(*d*,*e*).

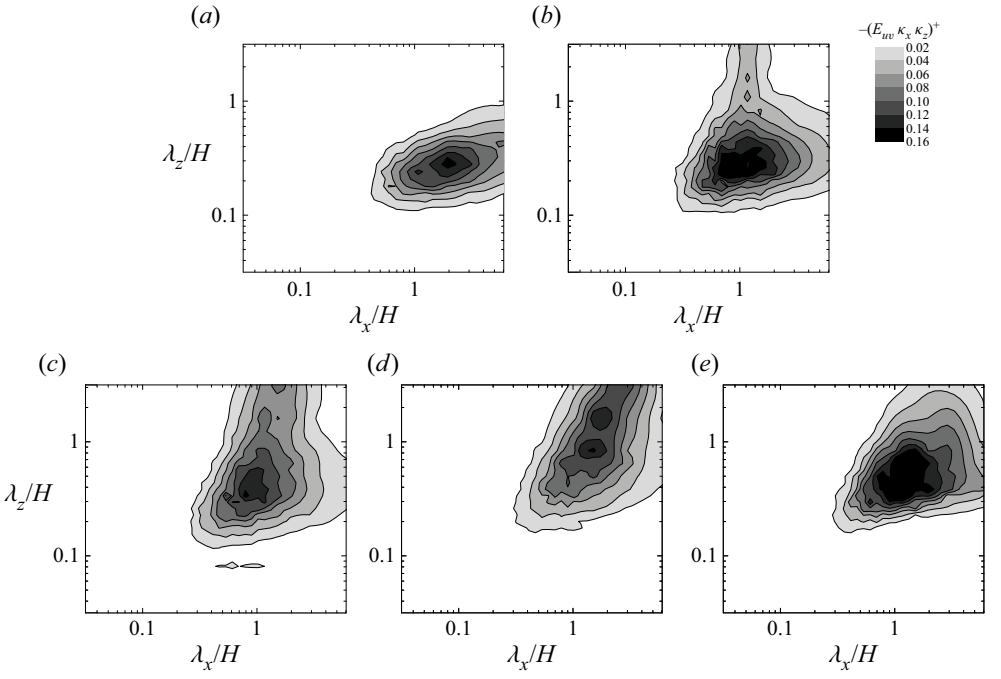


Figure 9. Two-dimensional pre-multiplied cospectra of the Reynolds shear stress at $y^+ \simeq 10$ for (*a*) the smooth wall case, (*b*) $s/h = 0.05$, (*c*) $s/h = 0.075$, (*d*) $s/h = 0.2$, and (*e*) $s/h = 0.45$.

Notably, the spectral map for $s/h = 0.05$ in figure 9(*b*) is similar to that for turbulent flows over drag-increasing riblets where the frictional resistance is increased due to the presence of spanwise rollers (Garcia-Mayoral & Jiménez 2012; Endrikat *et al.* 2021); however, the corresponding streamwise wavelength range for $s/h = 0.05$ ($300 < \lambda_x^+ < 600$) is somewhat larger than the reported range of the spanwise rollers ($65 < \lambda_x^+ < 290$) for the riblet flows (Garcia-Mayoral & Jiménez 2012). A possible explanation for the discrepancy is the difference in the rib geometry. Indeed, Endrikat *et al.* (2021) showed that the streamwise wavelengths that were affected by the spanwise rollers increased with increasing riblet size. We can assume that the reported range $2 < \lambda_x/H < 5.5$ for a porous-walled turbulent channel (Kuwata & Suga 2017, 2019; Suga *et al.* 2018) may be the maximum possible size of the spanwise rollers confined by the channel walls, and the smaller spanwise rollers may develop immaturely in slightly drag-increasing flows over rib roughness. The one- and two-dimensional cospectra suggest that spanwise rollers associated with the K–H instability develop for all rib cases; the weak and immature spanwise rollers develop for $s/h = 0.05$ and 0.075, and the fully developed spanwise rollers are sustained at $s/h = 0.2$ where the *RA* value attains the maximum peak value. The spanwise rollers are less organized for $s/h = 0.45$, probably resulting from increased flow disturbance near the rib crest. Given that the difference in $-R_{12}^+$ and $-H_2^+$, which is the primary source of the favourable breakdown of the Reynolds analogy, arises in the spectral space that is enhanced by the spanwise rollers, the favourable breakdown of the Reynolds analogy is connected closely to the presence of spanwise rollers.

The dissimilar temperature and velocity fluctuations induced by the spanwise rollers can be observed from the visualization of the streamwise velocity and temperature fluctuations

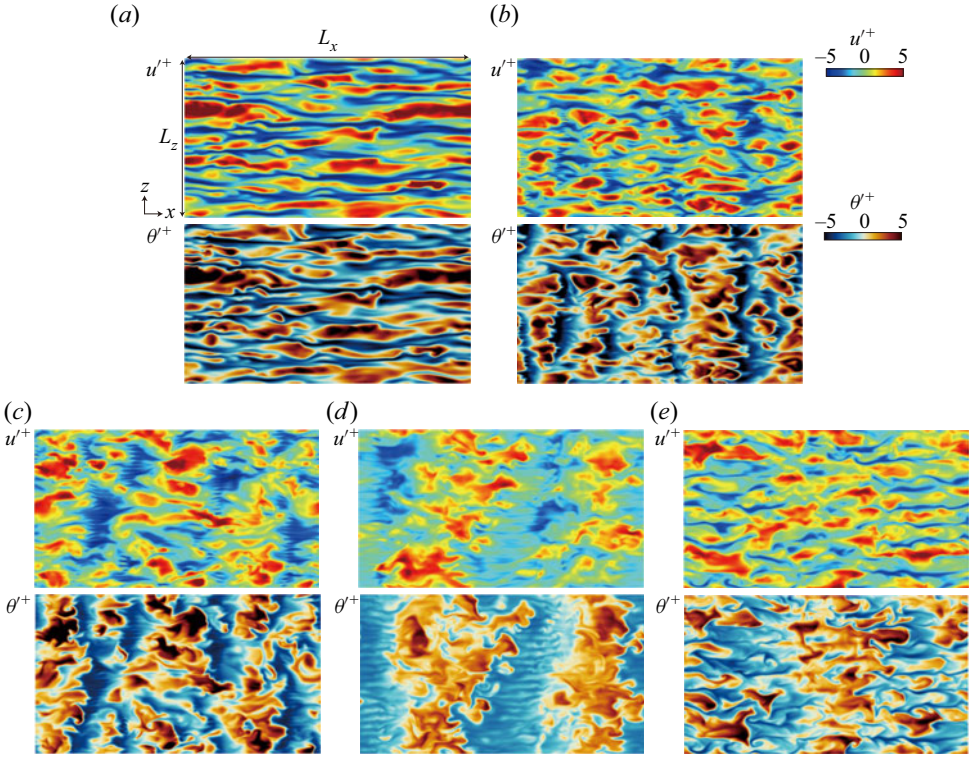


Figure 10. Snapshots of fluctuating velocity and temperature at $y^+ \simeq 10$ for (*a*) the smooth wall case, (*b*) $s/h = 0.05$, (*c*) $s/h = 0.075$, (*d*) $s/h = 0.2$, and (*e*) $s/h = 0.45$.

displayed in figure 10. The streamwise-elongated high- and low-speed streaks develop near the smooth wall, as shown in figure 10(*a*), whereas the streamwise-alternating high- and low-speed regions, which have strong spanwise coherence, are found for the rib cases in figures 10(*b–e*). For the rib cases, the wavelength of the streamwise perturbation increases with the $s/h$ value, and turbulence is dominated eventually by relatively large spanwise rollers for $s/h = 0.2$ in figure 10(*c*). These observations are consistent with the energy spectra in figures 8 and 9. It is worth noting that the turbulence structure for $s/h = 0.2$ is visually similar to the active-controlled near-wall flow by travelling-wave-like blowing/suction from the wall, which achieved substantial favourable breakdown of the Reynolds analogy (Hasegawa & Kasagi 2011; Yamamoto *et al.* 2013; Kaithakkal *et al.* 2020). An inspection of the temperature fluctuations confirms that the high (low)-temperature regions are found preferentially in the high-speed (low-speed) region, and the interfaces between the high- and low-temperature regions are visually sharper. More noticeable is that the streamwise-alternating patterns are more distinct for temperature fluctuations than velocity fluctuations, suggesting that the spanwise rollers affect temperature fluctuations more than velocity fluctuations.

Note that the origin of the spanwise rollers is the inflection point of the mean velocity just above the rib top; however, the effects of the spanwise rollers are not confined near the rib top. For turbulent flows over porous walls, it was reported that the spanwise rollers dominate the boundary layer and even affect the turbulence in the logarithmic region (Kuwata & Suga 2019; Kuwata 2022). Moreover, Kuwata & Suga (2016*a*) reported

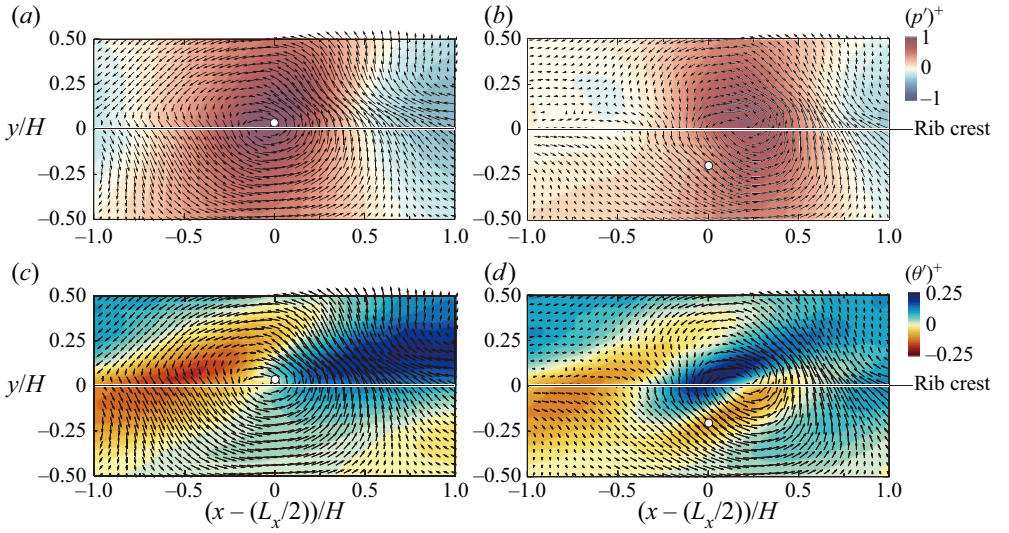


Figure 11. Contour maps of conditional average statistics along with the cross-sectional velocity vector for $s/h = 0.2$: (*a*,*c*) results with the reference point $(x, y, z) = (L_x/2,\ 10\nu/u_\tau,\ L_z/2)$; (*b*,*d*) results with the reference point $(L_x/2,\ -0.2H,\ L_z/2)$. Panels (*a*,*b*) show the pressure fluctuations, and (*c*,*d*) show the temperature fluctuations. The reference point is denoted by an open circle.

that the large-scale perturbations associated with the spanwise rollers do not decay deep inside the porous wall even where the small-scale turbulent fluctuations are dissipated. Similarly, for the present flows, the effects of the spanwise rollers, i.e. breakdown of the analogy between the heat and momentum transfer, are not confined near the top of the ribs. Indeed, $-H_2^+$ outweighs $-R_{12}^+$ even near the bottom of the ribs, as shown figure 5, and $\alpha_T^+$ outweighs $\nu_T^+$ further away above the top of the ribs, as can be seen in figure 7.

To provide a physical explanation for the reason why the spanwise rollers lead to the favourable breakdown of the Reynolds analogy, we analyse the conditional average statistics. The study focuses on the flow structures that affect directly the favourable breakdown of the Reynolds analogy. Thus the ensemble average is obtained for the snapshots that include the local favourable dissimilarity of the turbulent fluxes at the reference point. Specifically, we accumulate the snapshots that satisfy the inequality $-(v'\theta')^+ > -(u'v')^+$ at the reference point and apply ensemble average for those accumulated snapshots. We select the following two reference points: one point is just above the rib crest at $(x, y, z) = (L_x/2,\ 10\nu/u_\tau,\ L_z/2)$, and the other point is below the rib crest at $(L_x/2,\ -0.2H,\ L_z/2)$. Figure 11 presents the conditional average pressure and temperature distributions in a centre $x$–$y$ plane along with the cross-sectional conditional average velocity vectors. Here, $[p']^+$ and $[\theta']^+$ in the figure are the conditional average pressure and temperature fluctuations, respectively. The first notable observation is that the events of $-(v'\theta')^+ > -(u'v')^+$ are accompanied by a recirculating flow whose vortex core locates just above the rib crest. Since almost identical recirculating flow patterns are retained for both reference point cases, a single recirculating flow motion is responsible for the local favourable breakdown at two reference points. Moreover, this recirculating flow pattern is retained in the other $x$–$y$ plane at various $z$ locations (the results are not shown here). Thus the recirculating flow has two-dimensional

roller structure, which indicates that the recirculating flow can be considered as the footprint of the spanwise rollers. The inspection of the velocity vectors reveals that the events $-(v'\theta')^+ > -(u'v')^+$ at the reference point of $y^+ \simeq 10$ in figure 11(*a*) could be attributed to the spanwise-rollers-induced ejection, whereas those at $y = -0.2H$ in figure 11(*b*) could be attributed to the spanwise-rollers-induced sweep. As shown in figures 11(*c*,*d*), the spanwise-rollers-induced ejection and sweep motions convect the low- and high-temperature fluid, respectively, which generates a positive $-H_2^+$ value. Similarly, those motions generate a positive $-R_{12}^+$; however, near the reference points, the pressure gradient along the sweep and ejection motions is generally positive, which reveals that the ejection and sweep motions are suppressed by pressure. That is, generation of a positive $-R_{12}^+$ tends to be inhibited by the pressure gradient term, which appears in the momentum equation but not in the energy equation. This is the reason why the spanwise rollers lead to the local favourable breakdown of the Reynolds analogy. Spanwise rollers lead to a substantial enhancement of the pressure perturbation (Kuwata & Suga 2016*b*). The maximum peak value of the root-mean-square of the pressure fluctuations $p_{rms}^+$ for $s/h = 0.2$ is $p_{rms}^+ = 5.3$, which is increased by a factor 2.4 from the smooth wall case. This result may be another implication that the pressure fluctuations play a crucial role in the momentum transfer for porous wall turbulence. Finally, it should be noted that the present results do not imply that the favourable breakdown of the Reynolds analogy can always be achieved for porous wall turbulence because porous media typically offer substantial pressure drag. Thus the Reynolds analogy is usually broken in the unfavourable manner for turbulent heat transfer over porous media, as presented from the data by Nishiyama *et al.* (2020) in figure 2.

## 4. Conclusions

To study the favourable breakdown of the Reynolds analogy by the spanwise rollers associated with the K–H instability, we performed DNS of turbulent heat transfer over high-aspect-ratio streamwise-aligned longitudinal ribs at the friction Reynolds number 300. The temperature was assumed as a passive scalar with Prandtl number unity to discuss the similarity between the heat and momentum transfer. The high-aspect-ratio longitudinal ribs lead to the favourable breakdown of the Reynolds analogy, that is, the Reynolds analogy factor exceeds unity. The maximum Reynolds analogy factor $RA = 1.45$ is attained when the separation between the neighbouring ribs is 0.2 times as large as the rib height. The favourable breakdown of the Reynolds analogy is dominantly attributed to the enhanced turbulent heat flux compared with the Reynolds shear stress, whereas the rib-induced secondary mean flow plays a role in diminishing the favourable breakdown of the Reynolds analogy. The conditional average statistics reveals that the high-pressure region, which is accompanied by the spanwise rollers, suppresses the sweep and ejection motions, which results in the smaller Reynolds shear stress than the turbulent heat flux.

In this study, only flows with a single Prandtl number at a single Reynolds number were considered, and the solid rib ideally has a constant wall temperature with the assumption of the infinite conductivity. However, considering that the spanwise rollers associated with K–H instability, which primarily cause the favourable breakdown of the Reynolds analogy, develop over various types of porous walls at various Reynolds numbers, the passive flow control by spanwise rollers may be used in numerous practical applications. In addition, there is probably room for improvement of the heat transfer performance in the geometric configuration of the ribs, which will be the focus of our future work.

**Funding.** The author expresses their gratitude to their colleagues PhD K. Suga and Dr M. Kaneda for their support. A part of this study was supported financially by JSPS Japan (no. 21H01266). The numerical calculations were carried out on the TSUBAME3.0 supercomputer in the Tokyo Institute of Technology.

**Declaration of interests.** The author reports no conflict of interest.

**Author ORCIDs.**
Y. Kuwata https://orcid.org/0000-0002-9489-2788.

## References

ALBEN, S. 2017 Improved convection cooling in steady channel flows. *Phys. Rev. Fluids* **2** (10), 104501.

BONS, J.P. 2002 St and $c_f$ augmentation for real turbine roughness with elevated freestream turbulence. In *ASME Turbo Expo 2002: Power for Land, Sea, and Air*, pp. 349–363. American Society of Mechanical Engineers.

BRETHOUWER, G. 2021 Much faster heat/mass than momentum transport in rotating Couette flows. *J. Fluid Mech.* **912**, A31.

BREUGEM, W.P., BOERSMA, B.J. & UITTENBOGAARD, R.E. 2006 The influence of wall permeability on turbulent channel flow. *J. Fluid Mech.* **562**, 35–72.

DIPPREY, D.F. & SABERSKY, R.H. 1963 Heat and momentum transfer in smooth and rough tubes at various Prandtl numbers. *Intl J. Heat Mass Transfer* **6** (5), 329–353.

ENDRIKAT, S., MODESTI, D., GARCÍA-MAYORAL, R., HUTCHINS, N. & CHUNG, D. 2021 Influence of riblet shapes on the occurrence of Kelvin–Helmholtz rollers. *J. Fluid Mech.* **913**, A37.

FOROOGHI, P., STRIPF, M. & FROHNAPFEL, B. 2018 A systematic study of turbulent heat transfer over rough walls. *Intl J. Heat Mass Transfer* **127**, 1157–1168.

GARCIA-MAYORAL, R. & JIMÉNEZ, J. 2012 Scaling of turbulent structures in riblet channels up to $Re_\tau \simeq$ 550. *Phys. Fluids* **24** (10), 105101.

HASEGAWA, Y. & KASAGI, N. 2011 Dissimilar control of momentum and heat transfer in a fully developed turbulent channel flow. *J. Fluid Mech.* **683**, 57–93.

HINZE, J.O. 1973 Experimental investigation on secondary currents in the turbulent flow through a straight conduit. *Appl. Sci. Res.* **28** (1), 453–465.

HWANG, S., DONG, K., HYUN, G. & CHO, H.H. 2008 Heat transfer with dimple/protrusion arrays in a rectangular duct with a low Reynolds number range. *Intl J. Heat Fluid Flow* **29** (4), 916–926.

JIN, Y. & HERWIG, H. 2014 Turbulent flow and heat transfer in channels with shark skin surfaces: entropy generation and its physical significance. *Intl J. Heat Mass Transfer* **70**, 10–22.

KAITHAKKAL, A.J., KAMETANI, Y. & HASEGAWA, Y. 2020 Dissimilarity between turbulent heat and momentum transfer induced by a streamwise travelling wave of wall blowing and suction. *J. Fluid Mech.* **886**, A29.

KASAGI, N., HASEGAWA, Y., FUKAGATA, K. & IWAMOTO, K. 2010 Control of turbulent transport: less friction and more heat transfer. In *International Heat Transfer Conference*, vol. 49439, pp. 309–324.

KATOH, K., CHOI, K.-S. & AZUMA, T. 2000 Heat-transfer enhancement and pressure loss by surface roughness in turbulent channel flows. *Intl J. Heat Mass Transfer* **43** (21), 4009–4017.

KAYS, W.M. & CRAWFORD, M.E. 1993 *Convective Heat and Mass Transfer*, 3rd edn. McGraw-Hill.

KUWATA, Y. 2021 Direct numerical simulation of turbulent heat transfer on the Reynolds analogy over irregular rough surfaces. *Intl J. Heat Fluid Flow* **92**, 108859.

KUWATA, Y. 2022 Role of spanwise rollers by Kelvin–Helmholtz instability in turbulence over a permeable porous wall. *Phys. Rev. Fluids* **7** (8), 084606.

KUWATA, Y. & KAWAGUCHI, Y. 2019 Direct numerical simulation of turbulence over systematically varied irregular rough surfaces. *J. Fluid Mech.* **862**, 781–815.

KUWATA, Y. & NAGURA, R. 2020 Direct numerical simulation on the effects of surface slope and skewness on rough-wall turbulence. *Phys. Fluids* **32** (10), 105113.

KUWATA, Y. & SUGA, K. 2016*a* Lattice Boltzmann direct numerical simulation of interface turbulence over porous and rough walls. *Intl J. Heat Fluid Flow* **61**, 145–157.

KUWATA, Y. & SUGA, K. 2016*b* Transport mechanism of interface turbulence over porous and rough walls. *Flow Turbul. Combust.* **97** (4), 1071–1093.

KUWATA, Y. & SUGA, K. 2017 Direct numerical simulation of turbulence over anisotropic porous media. *J. Fluid Mech.* **831**, 41–71.

KUWATA, Y. & SUGA, K. 2019 Extensive investigation of the influence of wall permeability on turbulence. *Intl J. Heat Fluid Flow* **80**, 108465.

KUWATA, Y., TSUDA, K. & SUGA, K. 2020 Direct numerical simulation of turbulent conjugate heat transfer in a porous-walled duct flow. *J. Fluid Mech.* **904**, A9.

LIOU, T.-M., HWANG, J.-J. & CHEN, S.-H. 1993 Simulation and measurement of enhanced turbulent heat transfer in a channel with periodic ribs on one principal wall. *Intl J. Heat Mass Transfer* **36** (2), 507–517.

MACDONALD, M., HUTCHINS, N. & CHUNG, D. 2019 Roughness effects in turbulent forced convection. *J. Fluid Mech.* **861**, 138–162.

MAHMOOD, G.I, SABBAGH, M.Z. & LIGRANI, P.M. 2001 Heat transfer in a channel with dimples and protrusions on opposite walls. *J. Thermophys. Heat Transfer* **15** (3), 275–283.

MOTOKI, S., KAWAHARA, G. & SHIMIZU, M. 2018 Optimal heat transfer enhancement in plane Couette flow. *J. Fluid Mech.* **835**, 1157–1198.

MURATA, A. & MOCHIZUKI, S. 2001 Comparison between laminar and turbulent heat transfer in a stationary square duct with transverse or angled rib turbulators. *Intl J. Heat Mass Transfer* **44** (6), 1127–1141.

NAGANO, Y., HATTORI, H. & HOURA, T. 2004 DNS of velocity and thermal fields in turbulent channel flow with transverse-rib roughness. *Intl J. Heat Fluid Flow* **25** (3), 393–403.

NAKAYAMA, A., KUWAHARA, F. & KODAMA, Y. 2006 An equation for thermal dispersion flux transport and its mathematical modelling for heat and fluid flow in a porous medium. *J. Fluid Mech.* **563**, 81–96.

NISHIYAMA, Y., KUWATA, Y. & SUGA, K. 2020 Direct numerical simulation of turbulent heat transfer over fully resolved anisotropic porous structures. *Intl J. Heat Fluid Flow* **81**, 108515.

PEETERS, J.W.R. & SANDHAM, N.D. 2019 Turbulent heat transfer in channels with irregular roughness. *Intl J. Heat Mass Transfer* **138**, 454–467.

PIROZZOLI, S., BERNARDINI, M., VERZICCO, R. & ORLANDI, P. 2017 Mixed convection in turbulent channels with unstable stratification. *J. Fluid Mech.* **821**, 482–516.

POKRAJAC, D., FINNIGAN, J.J., MANES, C., MCEWAN, I. & NIKORA, V. 2006 On the definition of the shear velocity in rough bed open channel flows. In *Proceedings of the International Conference on Fluvial Hydraulics, 6–8 September 2006, Lisbon, Portugal* (ed. R.M.L. Ferreira, E.C.T.L. Alves, J.G.A.B. Leal & A.H. Cardoso), vol. 1, pp. 89–98.

STALIO, E. & NOBILE, E. 2003 Direct numerical simulation of heat transfer over riblets. *Intl J. Heat Fluid Flow* **24** (3), 356–371.

STROH, A., SCHÄFER, K., FOROOGHI, P. & FROHNAPFEL, B. 2020 Secondary flow and heat transfer in turbulent flow over streamwise ridges. *Intl J. Heat Fluid Flow* **81**, 108518.

SUGA, K., CHIKASUE, R. & KUWATA, Y. 2017 Modelling turbulent and dispersion heat fluxes in turbulent porous medium flows using the resolved LES data. *Intl J. Heat Fluid Flow* **68**, 225–236.

SUGA, K., MATSUMURA, Y., ASHITAKA, Y., TOMINAGA, S. & KANEDA, M. 2010 Effects of wall permeability on turbulence. *Intl J. Heat Fluid Flow* **31**, 974–984.

SUGA, K., OKAZAKI, Y., HO, U. & KUWATA, Y. 2018 Anisotropic wall permeability effects on turbulent channel flows. *J. Fluid Mech.* **855**, 983–1016.

YAMAMOTO, A., HASEGAWA, Y. & KASAGI, N. 2013 Optimal control of dissimilar heat and momentum transfer in a fully developed turbulent channel flow. *J. Fluid Mech.* **733**, 189–220.